A Novel Interferometric Microwave Radiometer Concept using Satellite Formation Flight for Geostationary Atmospheric Sounding

Ahmed Kiyoshi Sugihara El Maghraby, Angelo Grubišić, Camilla Colombo, Adrian Tatnall

***Abstract*—For most Earth observation applications, passive microwave radiometry from the geostationary orbit requires prohibitively large apertures for conventional single-satellite platforms. This article proposes a novel interferometric technique capable of synthesising these apertures using satellite formation flight. The significance of such concept is in its capacity to synthesise microwave apertures of conceptually unconstrained size in space for the first time. The technique is implemented in two formation flight configurations: a formation of a single full-sized satellite with microsatellites, and a formation of several full-sized satellites. Practical advantages and challenges of these configurations are found by applying them to geostationary atmospheric sounding at 53 GHz, the lowest sounding frequency considered for future sounder concepts GAS, GeoSTAR and GIMS. The two configurations produce apertures of 14.4 m and 28.8 m respectively using SMOS-sized satellites, and spatial resolution of 16.7 km and 7.5 km respectively from the geostationary orbit. The expected total mass are 1.3 and 4.0 tonnes respectively at the geostationary orbit. Inter-satellite ranging in micron-level precision is required. It is found that inter-satellite position uncertainty as small as 0.1 λ, 0.56 mm at 53 GHz, lead to up to 1.5 K error RMS in the reconstructed brightness temperature map. For other applications, the technique can be implemented at arbitrary microwave frequencies and arbitrary circular orbits, meaning it can also be used for other geostationary applications, or to achieve unprecedented spatial resolution at lower orbits, or to extend the accessible frequencies into the low radio waves for a variety of observables.**

I. Introduction

Passive microwave radiometry is a highly versatile tool for satellite remote-sensing of the Earth, producing a wide variety of meteorological and climate data products of both the surface and the atmosphere. Placing the instrument in the geostationary orbit has only recently become feasible using interferometric techniques demonstrated by the MIRAS instrument on board SMOS in 2009. [1] Ongoing research focuses on applying the technique to develop a geostationary sounder at higher microwave frequencies, for temperature and water vapour sounding from the geostationary orbit in order to significantly improve the accuracy of Numerical Weather Prediction (NWP).

Conventional geostationary weather satellites are equipped with optical and IR sensors, which are unable to provide sounding data under cloudy conditions. Microwave sounders on the other hand operate under all weather conditions and have been vital for NWP, however at the low Earth orbit temporal resolution is limited, where the current best is three hours by the GPM constellation. [2] For the significant improvement anticipated for the accuracy of NWP by introducing global real-time sounding, a full microwave sounding capability from the geostationary orbit is highly desired, and has been in consideration for the past number of years. [3]

Due to the diffraction limit, the aperture sizes necessary to achieve the required spatial resolution are prohibitive for conventional physical aperture techniques. Current research aims to synthesise these apertures using interferometric techniques, where major developments include radiometer concepts GeoSTAR (NASA, [4]), GAS (ESA, [5]) and GIMS (NSSC, China, [6]). These instruments however are all designed for single-satellite platforms, and the achievable aperture sizes are still fundamentally constrained by the satellite's physical size. If larger apertures are required, these may only be synthesised using a fleet of formation flying satellites.

In this article we propose to apply a novel interferometric technique, first described in [7], in which the available interferometric techniques are extended using satellite formation flight to further extend the achievable aperture sizes into such sizes that may not be achieved using single satellites. Two configurations applying this technique are simulated at 53 GHz, the lowest sounding frequency for the geostationary atmospheric sounder concepts, to explore the practical implications of formation flight interferometry.

The time is appropriate for such a technique to be discussed, since at the time of writing missions accomplished using satellite formation flight are growing, giving rise to new experience and techniques for sustained formation flight. To list a few examples, GRACE [8] and GRAIL [9] perform gravimetry with GRACE follow-on [10] planned, Tandem-X [11] performs bi-static radar with Tandem-L [12] planned, and the LISA [13] is a

planned gravitational wave antenna. The synthesis of microwave apertures has been in discussion as a possible application for satellite formation flight, and has been realised for active microwave missions with TanDEM-X. However formation flight for passive aperture synthesis is still unprecedented, and this is the topic of this article.

The significance of the proposed concept is in its capacity to synthesise microwave apertures of conceptually unconstrained size in space for the first time. The concept can be implemented at arbitrary microwave frequencies and arbitrary circular orbits, for a variety of observables. In addition to geostationary atmospheric sounding, the technique may also be applied to achieve unprecedented spatial resolution at lower orbits, or to extend the accessible frequencies into the low radio waves.

Section II introduces and develops the tools necessary to arrive at the suitable formation flight geometries. Section III applies these tools to size suitable constellations for geostationary atmospheric sounding. The simulated imaging performance of the concepts is presented in Section IV, and the performance degradation due to the deformation of formation flight is quantified in Section V, showing that micron-level inter-satellite ranging is required. A preliminary estimation for the total constellation mass is presented in Section VI.

II. Multi-Satellite Interferometric Radiometry

The purpose of radiometers is to map the brightness temperature of the observable scene at a specific microwave frequency so that useful meteorological information can be extracted from such maps. The diffraction limit defines the radiometer's angular spatial resolution as proportional to the ratio λ/D — the ratio between the instrument's centre frequency and its aperture size, usually diameter. This dictates that in order to place a radiometer in the geostationary orbit while maintaining the spatial resolution achievable in the low Earth orbit, an aperture approximately fifty-times larger is required. The interferometric techniques demonstrated by MIRAS may be directly applied on a multi-satellite architecture to synthesise these apertures.

An interferometer maps the scene brightness using a set of antennas which use a common local oscillator to down-convert their signals. In the case of multi-satellite interferometers this must be a set of synchronised oscillators that reside in each satellite. The size of the synthesised aperture is determined by the longest separation distance between the free-flying antennas. These separation distances are the baseline vectors, and must be measured at all times. A baseline vector is defined between each pair of antennas, and it is the separation vector between the phase centres of these antennas normalised by the wavelength, with components $[u, v, w]$ in the $[x, y, z]$ spatial dimensions with the $z+$ axis pointing towards the target. Under these conditions the signal waveform observed by each pair of antennas are cross-correlated to produce a point-sample measurement of an intermediate quantity called the visibility map, located at the baseline vectors $[u, v, w]$. The visibility map is related to the scene brightness temperature map as [14]

$$V = \iint^{\xi^2+\eta^2<1} \tilde{T}_B \hat{r} e^{-2\pi i(u\xi+v\eta+w\sqrt{1-\xi^2-\eta^2})} \mathrm{d}\xi \mathrm{d}\eta \quad (1)$$

where $V(u, v, w)$ is the visibility at baseline $[u, v, w]$, $\tilde{T}_B(\xi, \eta)$ is the modified brightness temperature map at the direction cosines $[\xi, \eta]$ and $\hat{r}$ is the fringe-washing function. $[\xi, \eta]$ are the direction cosines of the azimuth and elevation angles as measured from the $z+$ (nadir) axis, θ and ϕ respectively, and their use in place of the angles requires the modification of brightness temperature T_B by the obliquity factor, $\tilde{T}_B = T_B/\sqrt{1-\xi^2-\eta^2}$. With a planar array ($w = 0$) and negligible fringe-washing function ($\hat{r} = 1$), this expression collapses to the spatial Fourier transform of the modified brightness temperature map, hence the brightness temperature map can be retrieved using inverse Fourier transform.

Visibility measured between all possible pairs of antennas produce the visibility sampling pattern of the interferometer. The shape and size of the visibility sampling pattern are closely linked to the shape of the synthesised aperture, and is the key determinant of the imaging quality of the interferometer. A circular aperture is ideal for a clean image, [15] and this is achieved by mission concepts GAS and GIMS by physically rotating the array. [5], [6] The size of the samples reflects the size of the synthesised aperture, and consequently the spatial resolution. Since the sampling pattern is determined by the geometry of the formation flight, this motivates the search for a suitable set of formation flight geometries.

To explore the effect of formation flight on the visibility sampling pattern, first consider the array geometry and its sampling pattern of the monolithic Y-shaped array as adopted by the MIRAS instrument, shown in Figure 1. The modification of this pattern by the addition of free-flying antenna elements is now explored. Given the Y-shaped array, we propose two types of free-flying antennas that may be introduced: the free-flying single antenna and the identical copy of the given array. The effects of these two cases are shown in Figure 2 and 3 respectively, and are now discussed.

A. Single-Element Companions

Given an array of antennas, the addition of a single antenna at any distance away copies the geometry of the

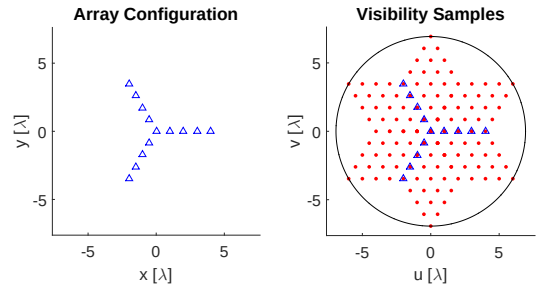

Fig. 1: Array geometry and sampling pattern of a 15-element Y-shaped interferometer. By rotating the array, all visibility within the circular bound can be sampled.

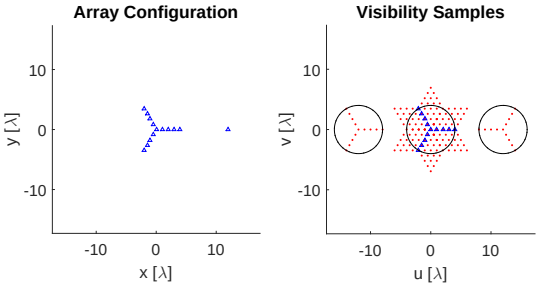

Fig. 2: Effect of introducing a single element to the array, shown in Figure 1, on the visibility sampling pattern.

array in the visibility sampling pattern at that distance. This is shown in Figure 2, where a Y-shaped visibility sample is introduced at the location of the single element. The advantage of this configuration is that these single elements may be flown on microsatellites that weigh a few tens of kilograms. Rotating the central array about the z axis also rotates the geometry of the array in the visibility space about their respective centres, which allowing circular visibility samples to be taken.

B. Array Duplication

Given an array of antennas, the introduction of an identical array at any distance copies of visibility sampling pattern of the individual array at the separation distance between the arrays. This is shown in Figure 3, where the separation of two identical Y-shaped arrays result in copies of the visibility samples separated at the same distance as between the arrays. The advantage to this configuration is its ability to synthesise larger apertures than the single-element companion configuration, at the cost of constellation total mass. Similarly, by rotating both arrays at the same direction and rate, both sampling patterns rotate about their respective centres.

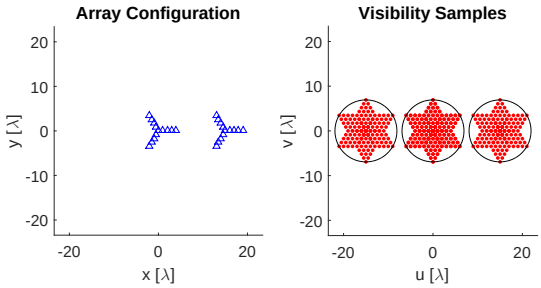

Fig. 3: Effect of introducing a duplicate of the array, shown in Figure 1, on the visibility sampling pattern.

III. Formation Geometries for Geostationary Atmospheric Sounding

The above effects are now applied to find suitable formation configurations that synthesise a single large circular aperture for geostationary microwave sounding. One scalable configuration is presented for each of the Single-Element Companions and the Array Duplication effects.

The mission is sized with the following considerations in mind. First, 53 GHz is chosen as the radiometer's centre frequency since this is the sounding frequency for atmospheric temperature, which is employed on GeoSTAR, GAS and GIMS, meaning direct comparison with these missions is possible. Furthermore the minimum baseline i.e. the minimum separation between antennas must be smaller than that specified by the Nyquist sampling criterion shown in Equation 2, determining the alias-free field of view θ_{AF} for a given minimum baseline b_{min} and wavelength λ.

$$\theta_{AF} = \frac{\lambda}{b_{min}} \tag{2}$$

This is the full field of view that must cover the entire Earth disc in order to prevent the aliases of the Earth from overlapping with one-another, making brightness readings in such regions unusable. The Earth is 17.4 degrees in diameter from the geostationary orbit, giving the minimum baseline of 3.29λ. A slightly smaller 3λ is chosen for the concepts discussed to include the cold space in the field of view, with total alias-free field of view amounting to 19.1 degrees. These antennas are distributed along rotating booms. To adhere to currently feasible satellite structures, 4 m booms are chosen, as already operational on the MIRAS instrument. With 3λ separation at 53 GHz, a boom of this length can accommodate 236 antenna elements.

A. The Single-Element Companion Concept

Applying the mechanism introduced in Section II-A, a set of Single-Element Companions are distributed around

a rotating main array in such a way that circular samples, seen in Figure 2, align in a hexagonal grid to completely fill the visibility space without gaps. The inter-satellite separation that allows this is $\sqrt{3}R$, where R is the length of each of the three booms in the Y-shaped array. At this separation the hexagonally latticed circular samples touch one another without gaps, synthesising the largest effective aperture. Larger separation will result in gaps between visibility samples, producing strong side-lobes, and smaller separation will result in redundant visibility overlap, leading to a smaller synthesised aperture. The result is shown in Figure 4a, in the nine-companion configuration. Each companion element (labled A to I) produces a pair of visibility samples with all elements in the central array. The samples shown in Figure 4b shows the visibility sample at one instant. By rotating the central array, each of these Y-shaped samples rotate about their centres, allowing each Y-shaped sample to obtain a circular visibility sample, as shown in Figure 4c, labelled with the companion satellite that produce these samples. The overlap of these circular samples produce the effective aperture, shown in the large circle. Visibility samples outside of this area are ignored to minimise side lobes and improve beam efficiency.

The resultant maximum baseline, which is the effective aperture diameter, is 3.6 times the arm length of the central Y-shaped array for the nine-companion option, producing an effective aperture of 14.4 m. This can be scaled larger by employing more companion satellites. Shown in Figure 5 is an 18-companion variant of the concept with 20.0 m aperture, and larger constellations up to the 63-companion variant are listed in Table I with their effective aperture sizes and achievable spatial resolution. Also shown are the total number of antenna elements and the required number of complex cross-correlators per sounding channel, at the number of baseline pairs. In the single-element companion concept no baseline redundancy is available, leading to the small number of required correlators. The number of baseline pairs listed in Table I compare to 10,000 pairs expected for GAS, which cover smaller visibility area. [16] To satisfy the sensitivity requirements at the given signal integration time, the number of baseline pairs can be increased by introducing additional elements on the companion satellites. All cross-correlators are located on the central satellite.

B. The Array Duplicate Concept

The second concept employs a constellation of six rotating two-boom interferometers flying in a triangular formation. For this particular formation the two-boom configuration allows for a larger aperture than the Y-shaped arrays. The inter-satellite distance in this concept is $2\sqrt{3}R$, which allows the circular visibility samples to

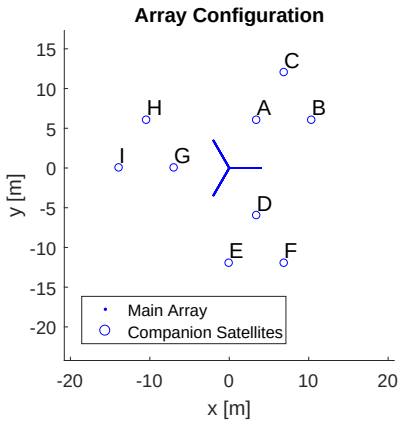

(a)

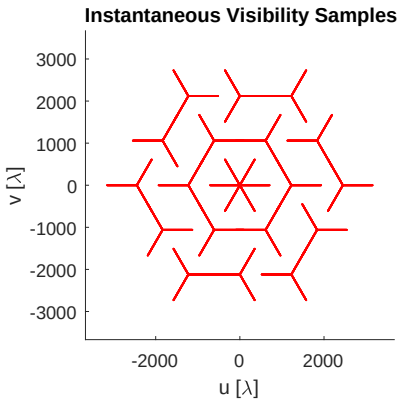

(b)

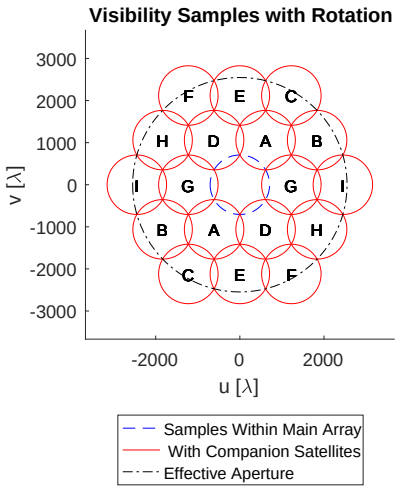

(c)

Fig. 4: A rotating Y-shaped interferometer flies in formation with nine microsatellites, each carrying single antenna elements A to I (a). The rotation leads to a circular effective aperture, the diameter of which is 3.6 times the length of the arms (c). Visibility samples at 53 GHz.

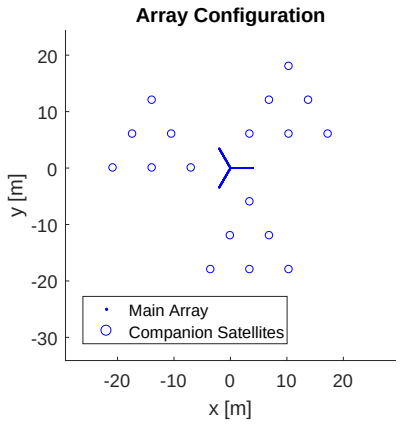

(a)

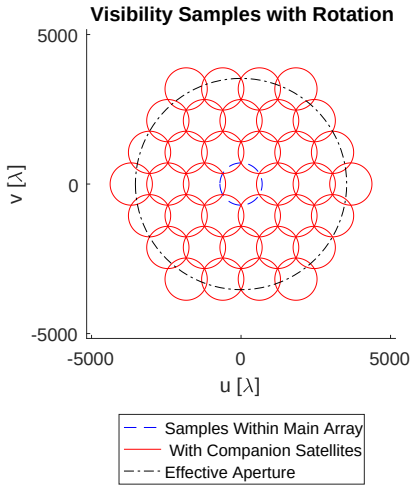

(b)

Fig. 5: An example of an up-scaled, 18-microsatellite configuration of the Single-Element Companion concept with increased effective aperture diameter of 5 times the length of the arms. Visibility samples at 53 GHz.

Comps	Aperture Diameter	S. Res	A.	Cor.
3	2.0 R = 8.0 m	30.1 km	711	2,832
9	3.6 R = 14.4 m	16.7 km	717	7,080
18	5.0 R = 20.0 m	12.0 km	726	13,452
30	6.5 R = 26.2 m	9.2 km	738	21,948
45	8.0 R = 32.0 m	7.5 km	753	32,568
63	9.6 R = 38.2 m	6.3 km	771	45,312

TABLE I: The scaling of the Single-Element Companion concept shown in Figure 4 for given number of companion satellites. The effective aperture with boom length R = 4 m and the resultant spatial resolution at 53 GHz is shown. Also shown are the total number of antenna elements and the correlators per channel.

overlap when the arrays are rotated, as shown in Figure 6. Despite the dissimilarity of the array configurations, the resultant visibility sampling pattern is identical to the first concept, as shown in Figure 8. This concept requires that all arrays rotate simultaneously, and the effective aperture is much larger at 28.8 m compared to the first concept at 14.4 m for the same boom length.

An important difference to the Single-Element Companion concept is the presence of redundant baseline pairs, which is absent in the former configuration. Shown in Figure 6b, the instantaneous visibility samples A can now be sampled independently by each individual array, resulting in five redundant measurements. Similarly, visibility samples B are sampled between arrays a and b, arrays f and a, and arrays e and c, resulting in two redundant measurements, and likewise for baselines C and D. Each of E and above have no redundant measurements for the nine-satellite formation. These redundant measurements represent six-fold increase in available signal integration time for A and three-fold for B to D, and translate to improved radiometric resolution for these visibility samples. The redundancies also improve the array's tolerance to uncertainties when measuring inter-satellite distances, as the average inter-satellite ranging error is zero. This is demonstrated in Section V.

The triangular constellation is also scalable for larger effective apertures. Shown in Figure 7 is the nine-satellite variant of the constellation, and the scaling up to the 18-variant configuration is summarised in Table II listing effective aperture and achievable spatial resolution, as well as the total number of antennas and correlators per sounding channel. The redundant baselines mean that more correlators are needed for this concept, however these can be distributed between all satellites.

Sats	Aperture Diameter	S. Res	A.	Cor.
3	4.0 R = 16.0 m	15.0 km	1416	2,005,056
6	7.2 R = 28.8 m	8.4 km	2832	8,020,224
9	10.0 R = 40.0 m	6.0 km	4248	18,045,504
12	13.1 R = 52.5 m	4.6 km	5664	32,080,896
15	16.0 R = 64.0 m	3.8 km	7080	50,126,400
18	19.1 R = 76.3 m	3.1 km	8496	72,182,016

TABLE II: The scaling of the Array Duplicate concept shown in Figure 6 for given number of satellites. The effective aperture with boom length R = 4 m and the resultant spatial resolution at 53 GHz is shown. Also shown are the total number of antenna elements and the correlators per sounding channel.

IV. Visibility Inversion Algorithm

As described in Section II, the measurement taken by the interferometer is that of the visibility of the scene. In order to recover the brightness temperature map from

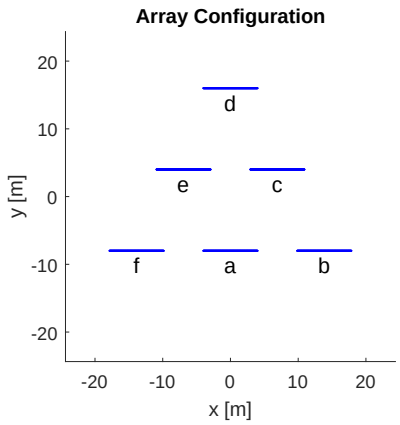

(a)

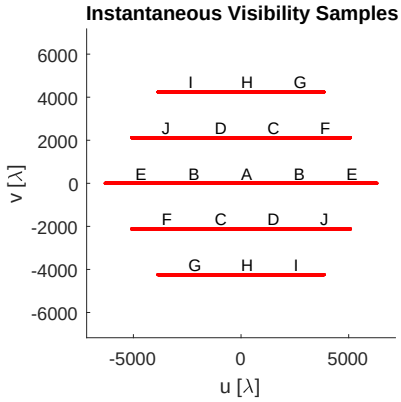

(b)

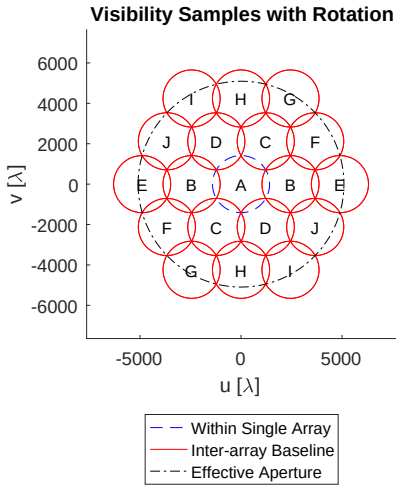

(c)

Fig. 6: Six-satellite configuration of the Array Duplicate concept with rotating two-boom interferometers. All booms rotate synchronously to develop a circular aperture with diameter of 28.8 m with 4 m booms. Visibility samples at 53 GHz.

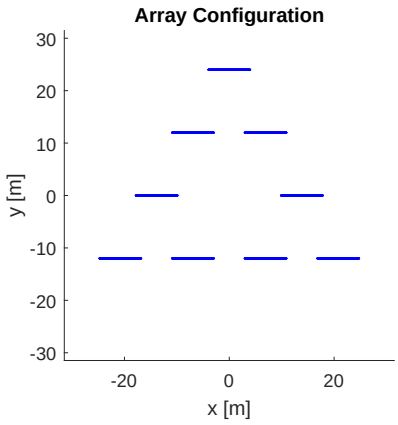

(a)

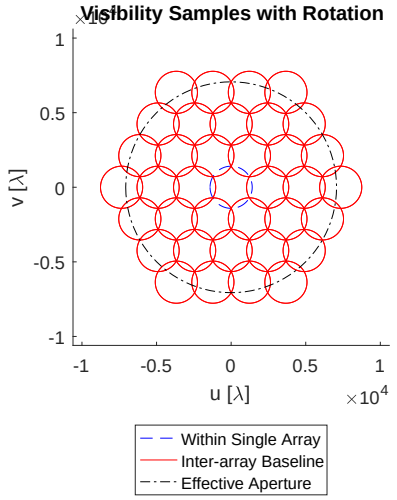

(b)

Fig. 7: An up-scaled nine-satellite configuration of the Array Duplicate concept with an effective aperture of 40 m with 4 m booms. Visibility samples at 53 GHz.

this measurement, the visibility must be inverted by an inversion algorithm. Had the visibility been measured in a regular Cartesian grid, such as rectangular or hexagonal grids, the inverse Fast Fourier Transform could have been used as it is done for MIRAS [17]. With the proposed rotating arrays however, the sampling grid is not Cartesian. We propose that the visibility is sampled on a variant of a polar grid, such that samples are taken at a regular angular interval — and therefore regular time interval— with the proposed rotating arrays. This allows equal signal integration time for each visibility sample. With such strategy an interlaced polar distribution emerges, as shown in Figure 8. The visibility samples are then directly inverted with a slower discrete method.

The modified brightness temperature $\tilde{T}_B$ is recovered by

$$\tilde{T}_B(\xi,\eta) = \sum_{i=1}^{N} V_i W_i G_i e^{2\pi i(u_i\xi + v_i\eta + w_i\sqrt{1-\xi^2-\eta^2})} \quad (3)$$

For N visibility samples where V_i, is the i-th visibility sample at its baseline vector $[u_i, v_i, w_i]$. This method is applicable to arbitrary array distribution, including that with non-zero w_i.

W_i is the windowing function applied to reduce the strength of the side-lobes and improve the efficiency of the beam, whereby improving the interferometer's sensitivity. In this study the Blackman window is used, which is the windowing function applied on MIRAS, defined as follows. [18]

$$W_i = 0.42 + 0.5\cos(\pi\rho_i) + 0.08\cos(2\pi\rho_i) \quad (4)$$

where $\rho_i = \sqrt{u_i^2 + v_i^2}/b_{max}$ and b_{max} is the maximum baseline and effective aperture.

G_i is the density taper weighting function, and is equivalent to the differential area $\mathrm{d}u\mathrm{d}v$ in an inverse Fourier transform operation. For regular grids the sample density is constant, however for the proposed grid as shown in Figure 8, this must be computed for each visibility sample. For the proposed sampling pattern G_i is a product of two components, as follows

$$G_i = G_{ia} G_{ib} \quad (5)$$

where G_{ia} accounts for the polar distribution of the samples, and G_{ib} accounts for the overlaps between these polar samples.

G_{ia} is found as

$$G_{ia} = r\delta r\delta\theta \quad (6)$$

where r is the radial distance of the visibility samples to the centres of the circular samples, not the origin of the visibility, δr is the radial distance between successive visibility samples, and $\delta\theta$ is the angular distance between visibility samples.

Where these polar grids overlap, the weighting for these visibility samples must be divided by two.

$$G_{ib} = \begin{cases} \frac{1}{2} & \text{in overlap zone} \\ 1 & \text{otherwise} \end{cases} \quad (7)$$

The result is shown in Figure 8, where the linear increase of weighting with radial distance from centres can be seen as defined in Equation 6, while the halving of weighting is also seen in overlap zones, as defined in Equation 7.

Using the Blackman windowing function, the normalised beam pattern of the Single-Element Companion concept with nine companion satellites is numerically simulated at 53 GHz. The size of the array is summarised in Table III. The resultant beam pattern, i.e. the interferometer array factor is shown in Figure 9b, and the beam performance is shown in Table IV. The inner circle in Figure 9b shows the Half-Power Beam Width at 16.7 km diameter, and the outer circle shows the Main Beam Width at 40.8 km, both circular due to the circular visibility sample and the circular windowing function. The hexagonal pattern of side-lobes is due to the hexagonal arrangement of the circular sampling patterns, and the discontinuities defined in equation 7 at the boundaries between the overlapping regions, as well as the zeros present in 6 at the centres of each circular visibility samples. Given this beam pattern, the CLEAN algorithm can be applied to the raw reconstructed image to reduce brightness retrieval errors to an acceptable level. [19]

To quantify the performance of the array, Equation 3 is applied for a given input scene brightness temperature map. In this study a test input image has been derived from GOES13 imagery data, re-scaled in brightness such that brightness temperature levels fall between 250 K and

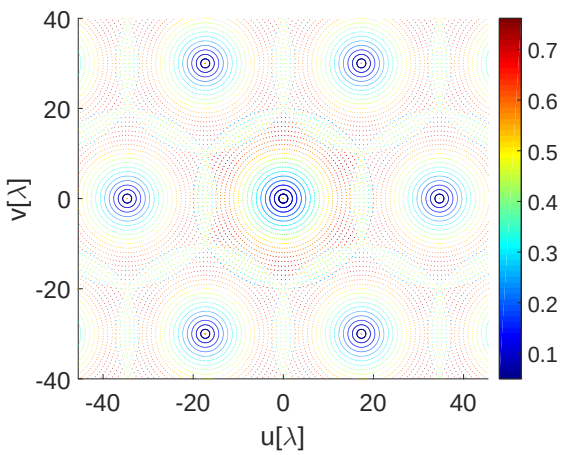

Fig. 8: The visibility sampling pattern obtained by the Single-Element Companion concept and the weighting functions associated to each point-sample. These values are calculated by Equation 5. The example uses a small array for clarity: 20 antenna elements per boom separated at 1 λ.

Parameter	Value
Boom Length	4 m
Minimum Baseline	3λ
Number of Antennas per Arm	236
Number of Companions	9
Maximum Baseline	14.4 m
Windowing Function	Blackman

TABLE III: Parameters of the simulated Single-Element Companion concept with nine companion satellites at 53 GHz. The beam produced by this array is shown in Figure 9b.

	Concept 1	Concept 2
-3dB Beam Efficiency	7.2%	
Main Beam Efficiency	11.9%	
-3dB Beam Width	16.7 km	8.3 km
Main Beam Width	40.8 km	20.4 km
Side-Lobe Level	-29 dB	

TABLE IV: Simulated beam performance of the Single-Element Companion (Concept 1) and the Array Duplicate (Concept 2) at 53 GHz from the geostationary orbit.

350 K, and cold sky brightness temperature is 2.73 K. This test image, shown in Figure 9a, is not representative of the brightness temperature map at 53 GHz, however it does enable the verification of the interferometer spatial resolution. First, the visibility samples are found by Equation 1. To perform this the input image is zero-padded and transformed via Fast Fourier Transform. The Fourier transform is then interpolated at the visibility sampling points shown in Figure 8. The interpolated visibility samples are then inverted using Equation 3. This produces the raw output, shown in Figure 9c with a spatial resolution of 16.7 km at 53 GHz. The first alias is clearly visible as a strong negative ring just outside the Earth disc, beyond which the aliased texture of the Earth is visible. Figure 9e shows the error, and it can be seen that the raw output is corrupted by the first alias of the dirty main beam. Since the raw image is the input image convolved with the dirty beam, the CLEAN algorithm can be used to deconvolve the raw image to reduce the error seen in Figure 9c, as described in [19] for the MIRAS instrument. The dirty beam, shown in Figure 9b, is assumed constant within the alias-free field of view. This beam, in conjunction with the a-priori knowledge on the horizon location and the assumed cold sky brightness temperature at 2.73 K, is used to iteratively clean the raw image until the root-mean-squared value of the residual within the alias-free field of view falls under 0.1 K. Note that due to the rotation of the arrays, the alias-free field of view is circular. The convergence occurred after 19 iterations for these trials. The result is then smoothed with a Blackman low-pass filter with the same beam width as the interferometer array factor. The deconvolved result is shown in Figure 9d with root-mean-squared error of 0.12 K within the Earth disc, error map found in Figure 9f.

The Array Duplicate concept produces an exactly identical visibility sampling pattern, and subsequently its beam performance is also identical to that of the Single-Element Companion concept, using the same inversion algorithm followed by the CLEAN process.

V. Effect of Uncertainties in Satellite Relative Positions

The visibility inversion process as described in Equation 3 requires the correct knowledge of the baseline vectors (u, v, w), which are the relative separation between antenna elements. With free-flying antenna elements, the uncertainties in the measurement of inter-satellite position will be a major source of error in the retrieved brightness temperature map.

The effect of these uncertainties have been calculated by simulating the array output with various levels of uncertainties in inter-satellite position measurements, at 0.01λ, 0.1λ and 1λ, and comparing them to the nominal output of the arrays. Here the physical baseline vectors include random inter-satellite position dislocations at the specified magnitude, and are used to determine the value of the visibility samples in Equation 1. The nominal baseline vectors are then used to recover the image using Equation 3.

The simulation results for the nine-companion Single-Element Companion concept (Concept 1) and the six-satellite Array Duplicate concept (Concept 2) are shown in Figures 10 and 11 respectively and summarised in Table V, where two simulations are performed, with in-plane and three-dimensional dislocations respectively. All outputs are processed by the CLEAN algorithm with 0.1 K as the threshold residual. To allow direct comparison between the Single-Element Companion and the Array Duplicate concepts, the two concepts are simulated at equal spatial resolution of 16.7 km, by reducing the boom-length of the Array duplicate option to 2 m.

It can be immediately seen that the out-of-plane deviation of the satellites have a larger impact than in-plane deviation in both cases, showing that inter-satellite ranging techniques sensitive to out-of-plane deviations will be instrumental to the proposed concepts. It can also be seen that the Array Duplicate concept, thanks to higher redundancy available in visibility samples, is more robust against deviations of satellite relative positions, in both in-plane and out-of-plane deviations.

The results show that the imaging performance of the constellation is highly sensitive to the errors in satellite relative position measurements, where an error as small as a tenth of a wavelength can lead to brightness temperature errors of 1.45 K RMS, and in 18% of the field of view the error is greater than 1 K. The orbital stability of the constellation is therefore a key determinant of the array performance, and micron-level measurement of inter-satellite relative position is required in both in-plane and out-of-plane directions at 53 GHz. Such precision is not unachievable, given the precision already achievable by GRACE at tens of microns, as well as the GRACE Follow-On mission planned to improve this by an order of magnitude. [20]

It is important to note that the cause of these errors is the uncertainties in measuring the inter-satellite relative positions, not the physical dislocation of the satellites

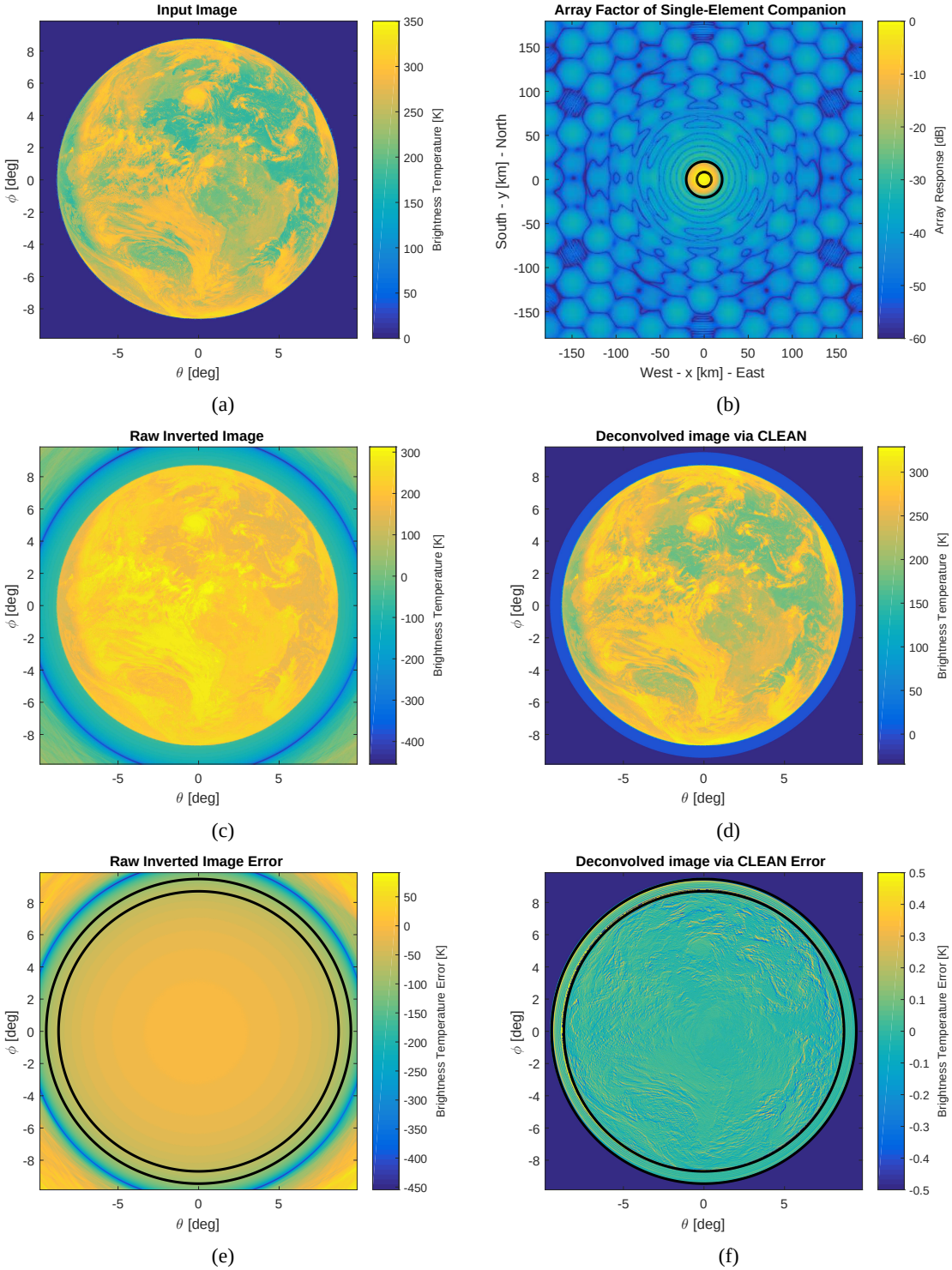

Fig. 9: Input image of the Earth from GEO (a), the image reconstructed by the Single-Element Companion interferometer at 53 GHz as described in Table III (c) using Equation 3, and the difference between a and c (e). To reduce the error the CLEAN algorithm has been applied, using the dirty beam (b), CLEAN result shown (d). Inner circle in 9b shows the Half-Power Beam Width, and the outer circle shows the first Null. The reduced error is shown (f). The location of Earth-sky horizon is at the inner circle in (e, f), and the interferometer field of view is the outer circle, within which the CLEAN operation is performed.

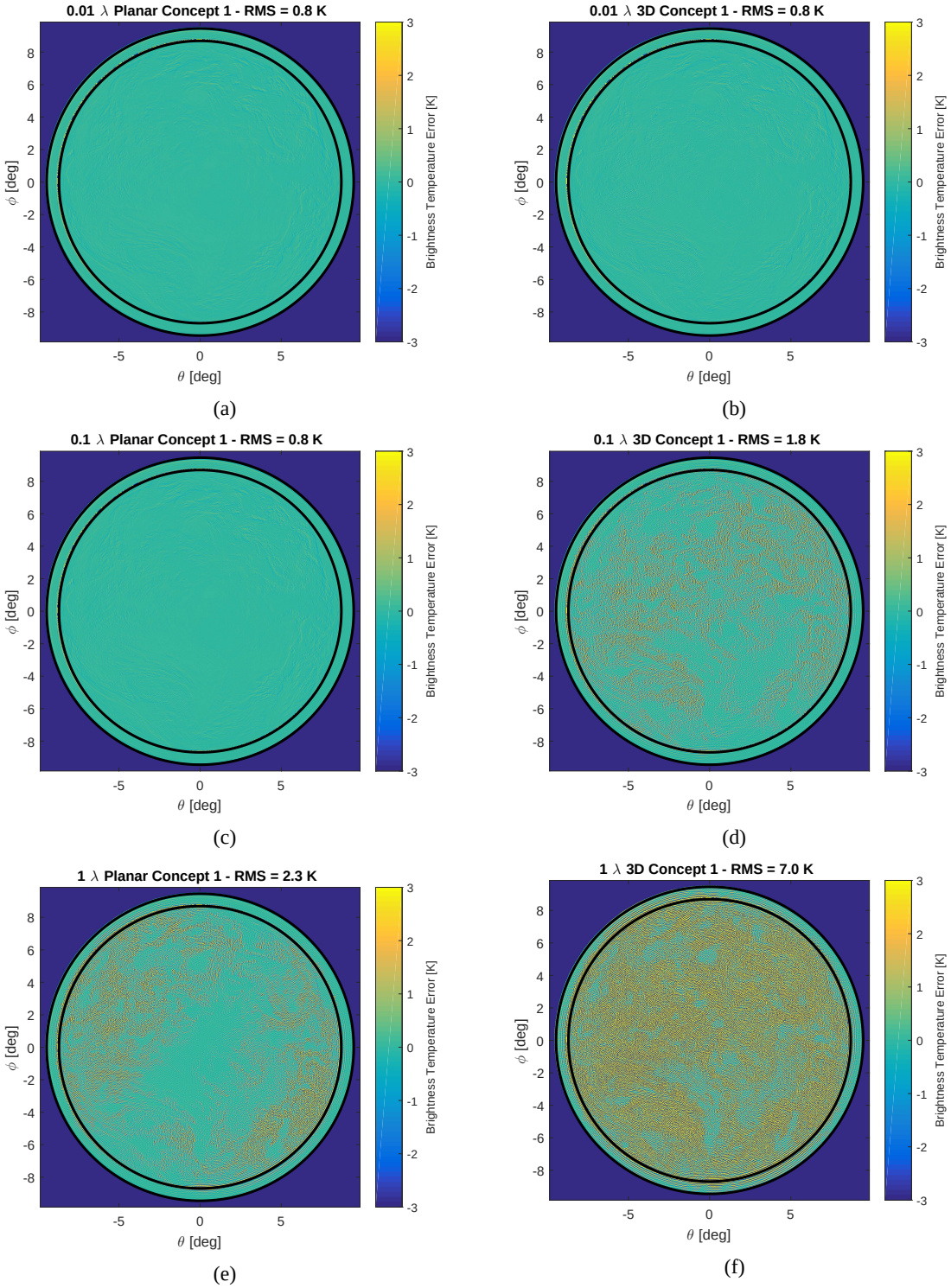

Fig. 10: Results on simulation trials on retrieved brightness temperature error due to inter-satellite position uncertainty of the Single-Element Companion concept by 0.01λ (a, b), 0.1λ (c, d), and 1λ (e, f). (a, c, e) show planar-only deviation, while (b, d, f) show planar and out-of-plane deviations. The inner circle shows the location of Earth-sky horizon, while the outer circle shows the area within which the CLEAN operation is performed.

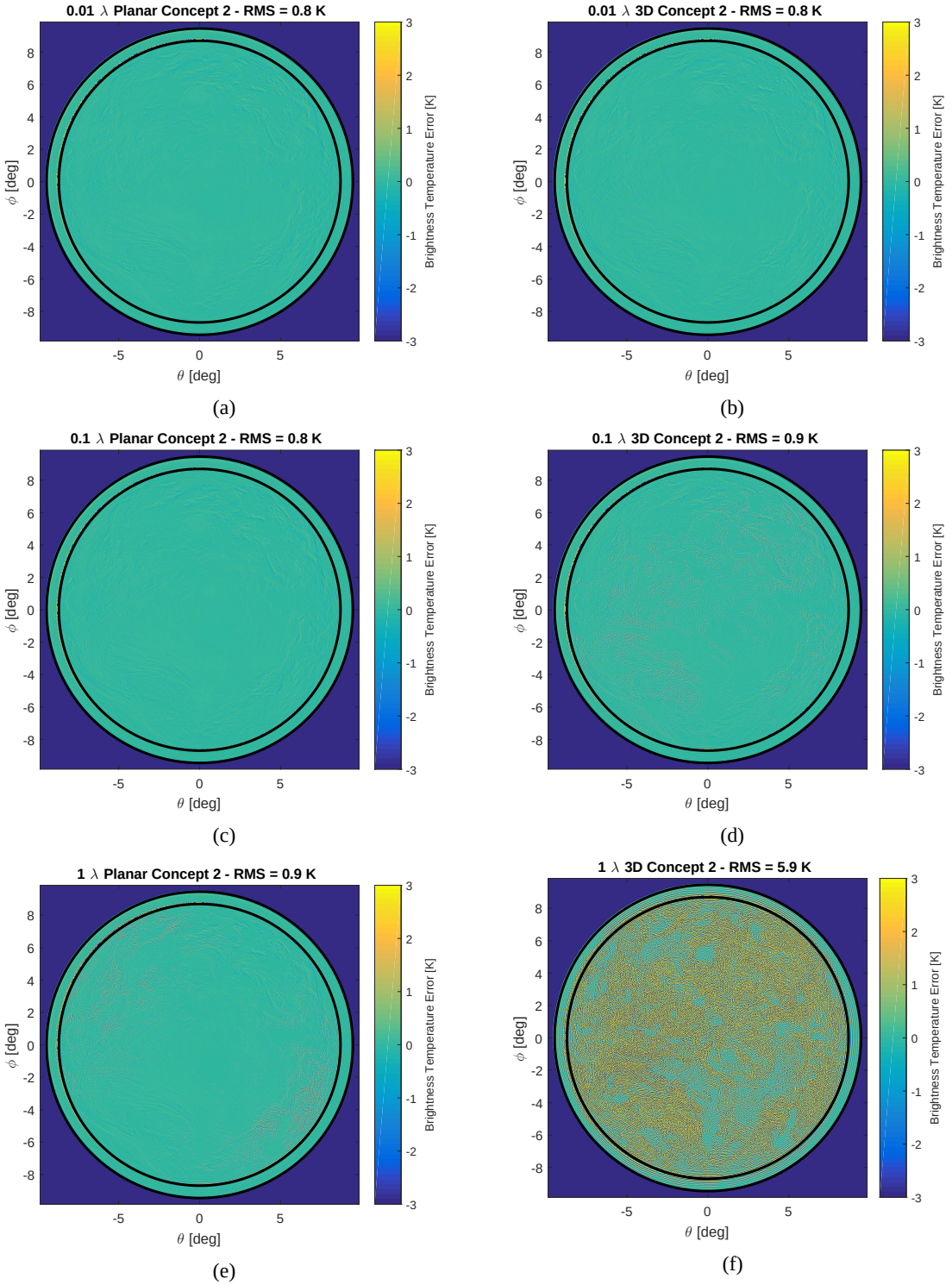

Fig. 11: Results on simulation trials on retrieved brightness temperature error due to inter-satellite position uncertainty of the Array Duplicate concept by 0.01λ (a, b), 0.1λ (c, d), and 1λ (e, f). The errors are lower than that found in the Single-Element Companion configuration (see Figure 10), due to the visibility sample redundancy available in the Array Duplicate configuration.

	Deviation [λ]	RMS Error [K]		Peak Error [K]	
Nominal	0	0.79	0.12	40.34	2.27
Concept 1	0.01	0.79	0.12	40.35	2.28
Planar	0.1	0.79	0.15	40.58	2.64
	1	2.26	1.78	60.34	24.59
Concept 1	0.01	0.79	0.16	40.42	2.84
3D	0.1	1.78	1.45	51.81	21.51
	1	7.01	6.32	92.89	76.28
Concept 2	0.01	0.79	0.12	40.32	2.25
Planar	0.1	0.79	0.13	40.35	2.50
	1	0.95	0.42	44.76	7.03
Concept 2	0.01	0.79	0.12	40.30	2.35
3D	0.1	0.90	0.42	40.94	5.26
	1	5.90	5.32	85.12	63.36
Concept 1 3D	3.5	2.87	0.95	74.92	24.49
Concept 2 3D	3.5	3.35	1.18	75.77	29.81

TABLE V: Results on simulation trials on retrieved brightness temperature error induced by inter-satellite position uncertainty as a function of uncertainty magnitude. Two error values are given for each uncertainty magnitude: first for the full field of view, and second for within Earth disc. Strong error present at horizon due to the Gibbs phenomenon. The last two rows show the errors at 3.5λ deviation which are measured without uncertainties.

itself. To demonstrate this another simulation has been run with 3.5λ deviation, approximately 2 cm deviation at 53 GHz, but with exact knowledge of satellite relative position. The resultant error, shown in Figure 12, are much less than that seen with 1λ deviation, shown in Figures 10f and 11f. The result is also summarised in Table V.

Although the error within the Earth disc for the known deviation of 3.5λ are still large at 0.95 K and 1.18 K RMS within the Earth disc for Single-Element Companion and the Array Duplicate concepts respectively, it is found that most of this error are at the Earth-sky horizon due to a strong Gibbs phenomenon. In fact, if we consider the area within 6.7 degrees from the origin, which is 79% of the Earth disc by diameter, the RMS errors drops to 0.31 K and 0.28 K RMS for the two concepts respectively.

Further it is important to note that the results presented in this section are produced by single trials of random deviations in satellite positions. Therefore further trials will produce differing results; as such these trials should only be seen as an indication to the expected magnitude of the retrieved brightness temperature error for each of the deviation magnitudes.

VI. Preliminary Estimation of Constellation Mass

To compute a first-order estimate for the total constellation launch mass for the presented concepts, the following assumptions are made. The central satellite for the Single-Element Companion concept, as well as all

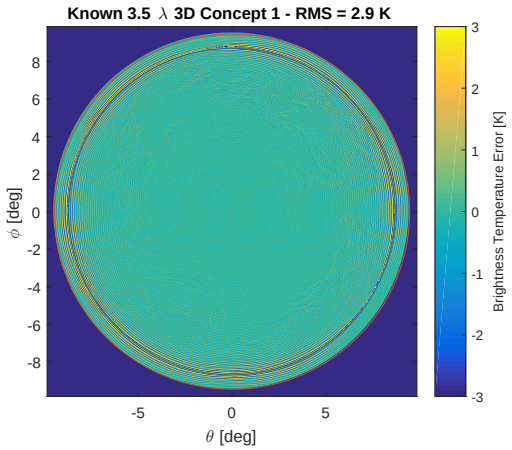

(a)

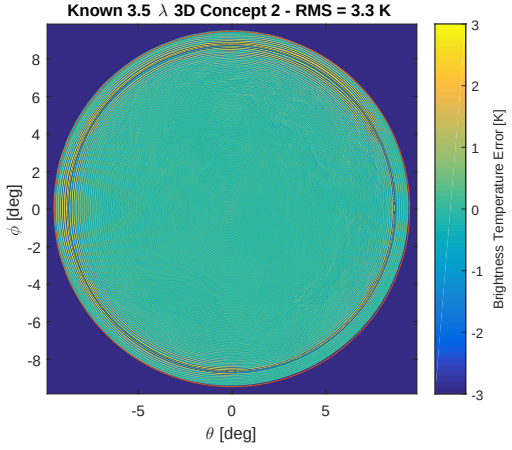

(b)

Fig. 12: Retrieved brightness temperature errors for Single-Element Companion (a) and Array Duplicate (b) with 3.5λ inter-satellite position deviation which are measured without uncertainties.

satellites for the Array Duplicate concepts are the same size as SMOS, are assumed to also weigh the same at 658 kg. For the Single-Element Companion concept, the mass of microsatellites are estimated using the payload-satellite mass ratio found in [21]. The payload for each satellite is a single receiver and a communication instrument with the central satellite, which should be at a few Mbps. At 53 GHz, the size of the antenna is a few centimetres in all dimensions, as used in GAS [5]. From this information the total payload mass of the microsatellite should be within 20 kg. Assuming payload-to-satellite mass ratio of 20% to 30%, the total mass of the microsatellite is 67 kg to 100 kg.

With this in mind, the estimated total constellation mass for both concepts are tabulated in Table VI. It can be seen that Array Duplicate concept, as it is a constellation of full-sized satellites, is considerably heavier.

Number of Companions	Aperture Diameter	Spatial Resolution	Mass
3	8.0 m	30.1 km	868 kg
9	14.4 m	16.7 km	1288 kg
18	20.0 m	12.0 km	1918 kg
30	26.2 m	9.2 km	2758 kg
45	32.0 m	7.5 km	3808 kg
63	38.2 m	6.3 km	5068 kg

(a) Constellation mass estimates for the Single-Element Companion concept

Number of Satellites	Aperture Diameter	Spatial Resolution	Mass
3	16.0 m	15.0 km	1974 kg
6	28.8 m	8.4 km	3948 kg
9	40.0 m	6.0 km	5922 kg
12	52.5 m	4.6 km	7896 kg
15	64.0 m	3.8 km	9870 kg
18	76.3 m	3.1 km	11844 kg

(b) Constellation mass estimates for the Array Duplicate concept

TABLE VI: First-order estimates for total constellation mass for the Single-Element Companion concept and the Array Duplicate concept, listed with the number of satellites, size of synthesised apertures and the achieved spatial resolution from the geostationary orbit

This suggests that while the Single-Element Companion concept e.g. the nine-companion configuration may be launched into the geostationary orbit using a heavy launch vehicle such as the Ariane 5, the Array Duplicate concepts may require multiple launches and rendezvous at the operational orbit, as few commercial launch vehicles are available to accommodate such payload to the geostationary orbit. [22] The total constellation mass per effective aperture diameter however are comparable for both concepts.

VII. Conclusion

A novel interferometric radiometer concept using satellite formation flight has been presented, and this has been applied to geostationary atmospheric sounding observing at 53 GHz to show the practical implications of such concept. While the geostationary sounder concepts GeoSTAR, GAS and GIMS are currently in development, the proposed formation flight concept introduces the capacity to synthesise apertures of conceptually unconstrained size in space for the first time. In addition to geostationary applications, such capability may be applied to achieve unprecedented spatial resolution at lower orbits, or to extend the accessible frequencies into the low radio waves.

Two viable variants of the radiometer concept has been explored. The first concept is the Single-Element Companion concept with a rotating Y-shaped interferometer flying in formation with several formation-flying microsatellites, achieving apertures of 14.4 m and larger. The second concept is the Array Duplicate concept with several medium-sized satellites flying in formation, which can synthesise apertures of 28.8 m and larger. These aperture sizes represent two-fold and four-fold improvement to the 7 m aperture synthesised by SMOS, and can be further increased by increasing the number of satellites.

The total mass of the constellation is expected to reach two tonnes and heavier, depending on the aperture size required. Particularly for the array duplicate configuration, where multiple full-sized satellites fly in formation, constellation total mass may exceed five tonnes.

The effect of uncertainties in measuring satellite relative position has been studied and presented in Section V. As a result the arrays have been found to be highly sensitive to the uncertainties in the measurement, where errors as small as a tenth of the wavelength can result in up to 1.5 K error RMS in the retrieved brightness temperature within the Earth disc. For this reason micron-level inter-satellite ranging is instrumental to such a mission. It has also been found that the presence of redundancy in baseline vectors improves the array's robustness against the uncertainties, where the Array Duplicate concept produced an error of 0.42 K RMS at 0.1 λ deviation.

VIII. Acknowledgments

This research has been funded by the UK Engineering and Physical Sciences Research Council (EPSRC). Award Reference number 1503202

References

[1] J. Font et al., "SMOS: The Challenging Sea Surface Salinity Measurement From Space," in *Proceedings of the IEEE*, vol. 98, no. 5, pp. 649-665, May 2010.

[2] Hou, A., R. Kakar, S. Neeck, A. Azarbarzin, C. Kummerow, M. Kojima, R. Oki, K. Nakamura, and T. Iguchi, "The Global Precipitation Measurement Mission" in *Bulletin of the American Meteorological Society*, vol. 95, no. 1, pp. 701–722, May 2014.

[3] U. Klein, Chung-Chi Lin, N. Atkinson, J. Charlton and C. Philpot, "Future microwave radiometers in geostationary and medium earth orbit," *IGARSS 2003. 2003 IEEE International Geoscience and Remote Sensing Symposium. Proceedings (IEEE Cat. No.03CH37477)*, 2003, pp. 2158-2160.

[4] B. Lambrigtsen, T. Gaier, P. Kangaslahti, B. Lim, A. Tanner and C. Ruf, "Enabling the NASA decadal-survey "PATH" mission," *2016 IEEE International Geoscience and Remote Sensing Symposium (IGARSS)*, Beijing, 2016, pp. 3949-3951.

[5] Christensen, J.; Carlström, A.; Ekstrom, H.; Emrich, A.; Embretsén, J.; de Maagt, P.; Colliander, A., "GAS: the Geostationary Atmospheric Sounder," in *Geoscience and Remote Sensing Symposium, 2007. IGARSS 2007.* IEEE International , vol., no., pp.223-226, 23-28 July 2007

[6] Hao Liu; Ji Wu; Shengwei Zhang; Jingye Yan; Lijie Niu; Cheng Zhang; Weiying Sun; Huiling Li; Bin Li, "The Geostationary Interferometric Microwave Sounder (GIMS): Instrument overview and recent progress," in *Geoscience and Remote Sensing Symposium (IGARSS), 2011* IEEE International , vol., no., pp.3629-3632, 24-29 July 2011

[7] A. K. Sugihara El Maghraby, A. Grubišić, C. Colombo, A. Tatnall, "A Novel Approach to Microwave Interferometric Radiometry in the Geostationary Orbit using Formation Flight," *IAC 2016. 67th International Astronautical Congress, Guadalajara, Mexico*, 2016.

[8] W. Zheng, H. Hsu, M. Zhong and M. Yun, "Precise Recovery of the Earth's Gravitational Field With GRACE: Intersatellite Range-Rate Interpolation Approach," in *IEEE Geoscience and Remote Sensing Letters*, vol. 9, no. 3, pp. 422-426, May 2012.
[9] D. G. Enzer, R. T. Wang and W. M. Klipstein, "GRAIL — A microwave ranging instrument to map out the lunar gravity field," *2010 IEEE International Frequency Control Symposium*, Newport Beach, CA, 2010, pp. 572-577.
[10] M. Stephens et al., "Demonstration of an Interferometric Laser Ranging System for a Follow-On Gravity Mission to GRACE," *2006 IEEE International Symposium on Geoscience and Remote Sensing*, Denver, CO, 2006, pp. 1115-1118.
[11] G. Krieger et al., "TanDEM-X: A satellite formation for high-resolution SAR interferometry," *2007 IET International Conference on Radar Systems*, Edinburgh, UK, 2007, pp. 1-5.
[12] A. Moreira et al., "Tandem-L: A Highly Innovative Bistatic SAR Mission for Global Observation of Dynamic Processes on the Earth's Surface," in *IEEE Geoscience and Remote Sensing Magazine*, vol. 3, no. 2, pp. 8-23, June 2015.
[13] K. Danzmann et al, "LISA — Laser Interferometer Space Antenna: A proposal in response to the ESA call for L3 mission concepts," Albert Einstein Institute, Hannover, Germany, 2017.
[14] I. Corbella, N. Duffo, M. Vall-llossera, A. Camps and F. Torres, "The visibility function in interferometric aperture synthesis radiometry," in *IEEE Transactions on Geoscience and Remote Sensing*, vol. 42, no. 8, pp. 1677-1682, Aug. 2004. DOI: 10.1109/TGRS.2004.830641
[15] Corbella, I.; Martin-Neira, M.; Oliva, R.; Torres, F.; Duffo, N., "Reduction of Secondary Lobes in Aperture Synthesis Radiometry," in *Geoscience and Remote Sensing Letters, IEEE*, vol.9, no.5, pp.977-979, Sept. 2012
[16] Jacob Christensen ; Anders Carlström ; Anders Emrich ; Peter de Maagt; "The Geostationary Atmospheric Sounder (GAS)." *Proc. SPIE 6361, Sensors, Systems, and Next-Generation Satellites X*, 636109 (October 03, 2006); doi:10.1117/12.689577.
[17] A. Camps, J. Bara, I. C. Sanahuja and F. Torres, "The processing of hexagonally sampled signals with standard rectangular techniques: application to 2-D large aperture synthesis interferometric radiometers," in *IEEE TRANSACTIONS ON GEOSCIENCE AND REMOTE SENSING*, vol. 35, no. 1, pp. 183-190, Jan 1997.
[18] A. Camps, "Application of Interferometric Radiometry to Earth Observation," Ph.D. dissertation, Department of Signal Theory and Communications, Polytechnic University of Catalonia, Barcelona, Spain, 1996.
[19] A. Camps, J. Bara, F. Torres, and I. Corbella. Extension of the clean technique to the microwave imaging of continuous thermal sources by means of aperture synthesis radiometers, 1998.
[20] W. Klipstein et al., "The GRACE Follow-On Laser Ranging Interferometer; A inter-spacecraft laser interferometry technology demonstrator with similarities to LISA," *APS April Meeting 2016*, Salt Lake City, UT, 2016.
[21] J. Wertz and W. Larson, *Space Mission Analysis and Design*, 3rd ed. Hawthorne,CA, Microcosm Press, 1992.
[22] Federal Aviation Administration, "The Annual Compendium of Commercial Space Transportation: 2016," January 2016

Ahmed Kiyoshi Sugihara El Maghraby obtained a Master of Engineering in Space Systems Engineering at the University of Southampton in 2014, working on an extremely low altitude satellite photogrammetry mission concept. He is currently a PhD student at the University of Southampton in the Astronautics Research Group. His research focus is in applying satellite formation flight to passive microwave interferometry, with particular interest in applying this to geostationary microwave radiometry for real-time observation of meteorological phenomena.

Angelo Grubisic was born in Walsall, England in 1981. He received his PhD from the University of Southampton and an MSc from the International Space University in 2009 and 2005 respectively. He has worked extensively on the development and testing of gridded ion thrusters and other electric propulsion systems, including the NSTAR ion thruster at NASA JPL and theT6 ion thruster for QinetiQ. From 2010 to 2013, he was responsible for designing and leading the systems level coupling and qualification tests for the Bepi Colombo electric propulsion system on the Mercury Transfer Module, the highest power dual ion thruster system to date. Since then, he has been pioneering selective laser melting additive manufacturing technologies for production of advanced propulsion systems as a lecturer within the Astronautics Group at the University of Southampton.

Dr Camilla Colombo is Associate Professor at Politecnico di Milano, where she leads a European Research Council Starting Grant on the project COMPASS "Control for Orbit Manoeuvring through Perturbations for Application to Space Systems". Her work spans orbital dynamics, space debris, high area-to-mass spacecraft, trajectory design and control and asteroid deflection and is published in 35 journal papers and 100 conference publications. She is involved in the EC funded project ReDSHIFT and contracts funded by the ESA. Between

2012 and 2016 she was working at the University of Southampton where she was lecturer of spacecraft system engineering courses run at ESA and lead research work on space debris and libration orbit missions. In 2013 she was appointed Research Fellow at Politecnico di Milano, sponsored by a Marie Curie Fellowship. Previously she worked as research fellow at the University of Strathclyde and Research Associate at the University of Glasgow, where she was awarded the William Wilson Scott Award Scholarship (2009) for her PhD thesis on "Optimal Trajectory Design for Interception and Deflection of Near Earth Objects". Camilla received her PhD from the University of Glasgow in 2010 and MEng in Aerospace Engineering from Politecnico di Milano in 2005.

Dr Tatnall graduated from Exeter University in 1973 and received a PhD from Sheffield University in 1978. He was a postdoctoral research assistant at York University and then a senior space systems engineer at British Aerospace. He joined the department of Aeronautics and Astronautics at Southampton University in 1988 and became Head of the Astronautics group at Southampton University and a Senior Tutor. His research has included internal waves, ocean colour, SAR ,formation flying and neural nets. In addition, he has been directly involved in the design and modelling of the performance of satellite passive microwave instruments. He was the organiser and lecturer of spacecraft system engineering courses run for industry at the European Space Agency and Southampton for 25 years. He has also authored chapters on systems engineering and telecommunications in the book "Space Systems Engineering" edited by Fortescue, Stark and Swinerd. For many years he served on the Space Committee of the UK Royal Aeronautical Society.